Water Practice & Technology

IWA PUBLISHING

Water Practice & Technology Vol 18 No 3, 647 doi: 10.2166/wpt.2023.021

Removal of cationic dyes from a synthetic effluent using a calcium surfactant

Yago Neco Teixeira [a,b,*], Francisco José de Paula Filho[a,b], Vinícius Pereira Bacurau[c], Jorge Marcell Coelho Menezes[a], Daniel Bernardes Silva[a], Jober de Queiroz dos Santos[a], Raimundo Nonato Pereira Teixeira[d] and João Victor Serra Nunes[e]

[a] Science and Technology Center, Federal University of Cariri, Av. Ten. Raimundo Rocha, 1639, Juazeiro do Norte, Ceará 63048-080, Brazil
[b] Agrarian Sciences and Biodiversity Center, Federal University of Cariri, Ícaro Moreira de Sousa St, 126, Crato, Ceará 63130-025, Brazil
[c] Materials Engineering Department, Federal University of São Carlos, Rod. Washington Luiz, 235, São Carlos, São Paulo 13565-905, Brazil
[d] Biological Chemistry Department, Regional University of Cariri, R. Cel. Antonio Luis, 1161, Crato, Ceará 63105-000, Brazil
[e] Physics Department, Federal University of Ceará, Pici Campus, 928, Fortaleza, Ceará 60440-900, Brazil
*Corresponding author. E-mail: yago.neco.teixeira@hotmail.com

YNT, 0000-0002-1538-4655

ABSTRACT

The present study aimed to evaluate the removal efficiency of two types of cationic dyes of different classes – methylene blue (MB) and malachite green (MG) – from a synthetic effluent using a calcium surfactant (CaSF) originated from used frying soybean oil. The Fourier Transform Infrared Spectroscopy (FTIR) spectra showed that the functional groups present on the surface of CaSF can form surface complexes or bonds with the dye molecules and, consequently, promote their adsorption. The adsorption kinetics studies indicated that the equilibrium point of the process is reached in 90 min for both dyes. Equilibrium studies indicated that the adsorption isotherm models that best fit MB and MG were the Langmuir and the Dubinin–Radushkevich models, respectively. The maximum adsorption capacities of MB and MG, according to the Langmuir model, were 199 and 123 $mg{\cdot}g^{-1}$, respectively. In the sight of the high MB and MG removal efficiency (84 and 100%, respectively), the use of CaSF is an excellent alternative for the treatment of effluents contaminated by cationic dyes. The adsorption–desorption cycle studies showed that CaSF maintains a good dye removal efficiency for up to three cycles.

Key words: adsorption, dyes, malachite green, methylene blue, surfactants

HIGHLIGHTS

- Calcium surfactant (CaSF) was manufactured from the frying soybean oil residues.
- CaSF is a good adsorbent for cationic dyes.
- CaSF was used to remove methylene blue (MB) and malachite green (MG) from synthetic effluent.
- CaSF has a high adsorption capacity (MB – 199 mg g^{-1}; MG – 123 mg g^{-1}).
- CaSF removed 84% of MB and 100% of MG.

GRAPHICAL ABSTRACT

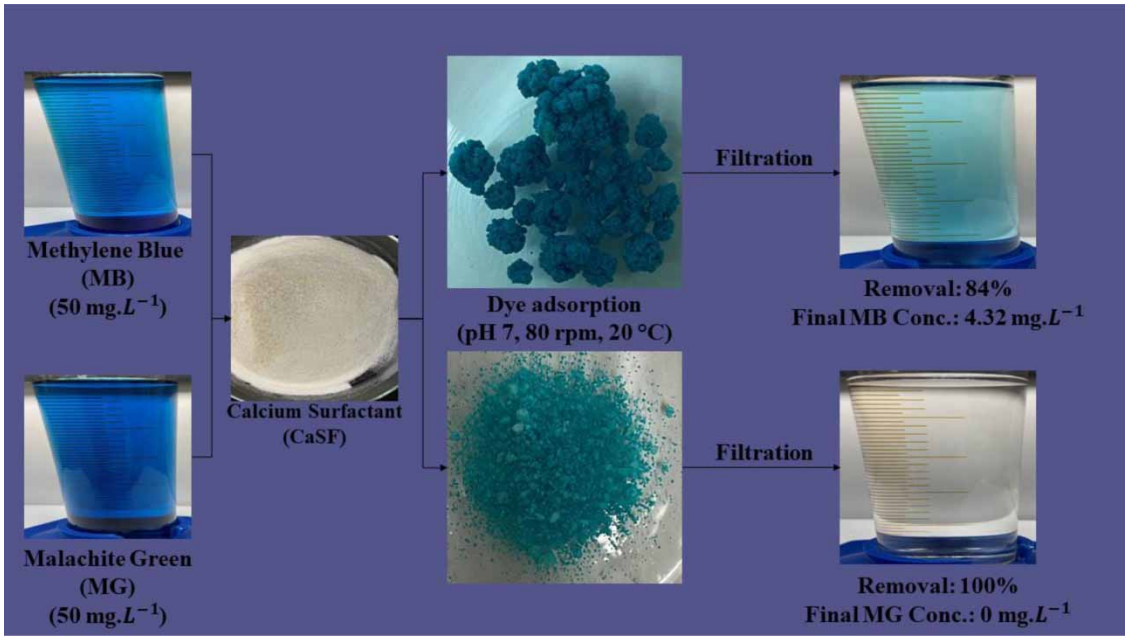

1. INTRODUCTION

Modern industrial operations use different types of dyes in routine processes, and industrial effluents containing excess dyes are harmful to the environment and human health.

In the environment, dyes, which are difficult to degrade, can interfere with natural processes by blocking the passage of light through the water, inhibiting photosynthesis, and affecting the growth of microorganisms and aquatic biota (Crini & Badot 2008; Anirudhan & Ramachandran 2015). In the case of human health, some dyes may have mutagenic and/or carcinogenic properties (Li *et al.* 2017; Mayani *et al.* 2017).

Methylene blue (MB) is a heterocyclic, cationic dye of the phenothiazine class used in the pharmaceutical, textile, plastic, cosmetics, leather, paper, and food industries (Peydayesh & Rahbar-Kelishami 2015). MB can cause increased pulse rate, shock, emesis, jaundice, cyanosis, and tissue necrosis (Zhou *et al.* 2015; Zhu *et al.* 2015).

Malachite green (MG) is a cationic dye of the triphenylmethane class, commonly used for dyeing wool, leather and paper, and as a fungicide, parasiticide and bactericide in aquaculture (Oyelude *et al.* 2018). MG is toxic and can accumulate in the tissues of animals that ingest water contaminated with it. It can cause the destruction of the liver, kidneys and intestine and is carcinogenic (Zhang *et al.* 2017).

Therefore, the efficient removal of dyes from effluents has been a hot research topic. Several types of processes are being studied for the treatment of effluents contaminated by these cationic dyes, namely precipitation (Lee *et al.* 2011), coagulation–flocculation (Yang *et al.* 2016), ion exchange (Sharma *et al.* 2016), photocatalysis (Khatri & Rana 2020), biological degradation (Sun *et al.* 2021), membrane filtration (Benosmane *et al.* 2022), and adsorption.

Adsorption is one of the most promising methods due to its simplicity, flexibility, efficiency and ability to sequester many compounds (Peydayesh & Rahbar-Kelishami 2015). Several types of adsorbents have been reported to be effective in removing MB and MG, such as kaolin (Mouni *et al.* 2018), biomass ash (Novais *et al.* 2018), nanochitosan (Salamat *et al.* 2019), composite hydrogel (Verma *et al.* 2020), activated carbon (Mariana *et al.* 2021), and biochar (Giri *et al.* 2022).

Surfactants are amphiphilic substances, widely used in effluent treatment (Petcu *et al.* 2016; Mortada 2020; Melo *et al.* 2021), and anionic surfactants the most widely used. The most common anionic surfactant is obtained by saponification of oils and/or fats and a strong base, such as sodium hydroxide (NaOH) or potassium hydroxide (KOH). This type of surfactant precipitates in the presence of calcium ions, forming calcium surfactant (CaSF). CaSF has a high affinity for organic compounds, being able to adsorb dyes.

CaSFs applied in effluent treatment have already been studied in coagulation–flocculation (Yang *et al.* 2016), micellar solubilization, and ionic flocculation (Melo *et al.* 2021; Teixeira *et al.* 2022a, 2022b). However, CaSF use as an adsorbent is novel; therefore, there are many aspects to investigate.

This study proposed to treat two synthetic effluents containing cationic dyes of different classes (MB and MG) as model pollutants. The study evaluated the dye removal efficiency using a CaSF obtained by means of an anionic surfactant originated from frying soybean oil, measuring the process kinetics, mechanism, and adsorption balance, as well as the morphology, functional groups and elemental composition of the CaSF. An attractive factor for the use of this CaSF, in addition to being easily obtained at a low cost, is its green and sustainable footprint.

2. MATERIALS AND METHODS

2.1. CaSF production

The CaSF used in this study was synthesized from an anionic surfactant and Ca^{2+} ions in an aqueous medium. The anionic surfactant was produced by saponification between frying soybean oil and NaOH (85.14 and 14.86% by mass, respectively). This ratio was based on the saponification index of the oil (154 g of oil and 26.88 g of NaOH). A 0.0625 M calcium chloride ($CaCl_2$) solution was used to provide the Ca^{2+} ions needed.

In a 5 L beaker, 20 g of the anionic surfactant was dissolved in 3.20 L of deionized water using a magnetic stirrer (100 rpm). After complete dissolution, 0.8 L of the 0.065 M $CaCl_2$ solution was added, and the stirring was reduced to 20 rpm for the formation of CaSF. CaSF flocs were filtered and oven-dried (50 °C, 6 h). After drying, the CaSF was macerated and sieved.

2.2. CaSF characterization

The CaSF surface characteristics, morphology and composition were analyzed by scanning electron microscopy (SEM) and energy-dispersive spectroscopy (EDS) using a scanning electron microscope (FEI, Inspect S50).

The CaSF was analyzed before and after dye adsorption by Fourier Transform Infrared Spectroscopy (FTIR) (PerkinElmer, Spectrum Two) to identify surface functional groups. The recorded spectra were in the range of 4,000–450 cm^{-1} at 4 cm^{-1} resolution using the potassium bromide (KBr) pellet method.

The point of zero charge (pH_{PZC}) was determined using the eleven-point methodology (Robles & Regalbuto 2004). A volume of 20 mL of these solutions was transferred to Erlenmeyer flasks containing approximately 20 mg of CaSF. The samples were shaken for a period of 6 h on a vibrating table (Nova Ethics, model 109). The pH of the solutions was measured and a graph of the final pH vs. initial pH was plotted to determine the pH_{PZC}.

2.3. Adsorption experiments

Separate stock solutions of MB ($C_{16}H_{18}ClN_3S = 319.85\ g{\cdot}mol^{-1}$) and MG ($C_{23}H_{25}ClN_2 = 364.91\ g{\cdot}mol^{-1}$) were prepared by dissolving 0.25 g of MB and MG in 0.5 L of deionized water. The adsorption experiments were carried out in batches, stirring the CaSF together with the MB or MG solutions. The concentrations of the MB and MG solutions, before and after adsorption, were determined using a UV spectrophotometer (Shimadzu, UV 1800) at a wavelength of 665 nm for MB and 617 nm for MG. The amount of dye adsorbed on the CaSF and the removal efficiencies were calculated using Equations (1)–(3), respectively.

$$q_t = \left(\frac{C_0 - C_t}{m}\right)V \tag{1}$$

$$q_e = \left(\frac{C_0 - C_e}{m}\right)V \tag{2}$$

$$\%\text{Efficiency} = \left(\frac{C_0 - C_e}{C_0}\right) \times 100 \tag{3}$$

where C_0, C_t and C_e are the concentrations of the dye at the initial time, at a given point in time, and at equilibrium, respectively ($mg{\cdot}L^{-1}$); q_t and q_e are the adsorption capacities at a given time and at equilibrium, respectively ($mg{\cdot}g^{-1}$); m is the mass of CaSF (g), and V is the volume of the solution (L).

2.4. Optimal conditions

The optimal values to promote dyes removal are shown in Table 1.

Table 1 | Optimum conditions for dye removal

Dye	MB	MG
CaSF dosage (g/L)	10	8
Stirring speed (rpm)	80	80
Equilibrium time (min)	90	90
pH	7	7
Temperature (°C)	20	20

2.5. CaSF dosage

The dosing effect was studied using varying concentrations of CaSF (1, 2, 4, 5, 8, 10, 15, 20 and 25 $g{\cdot}L^{-1}$) interacting with a 50 $mg{\cdot}L^{-1}$ MB or MG solution under optimal conditions (Table 1).

2.6. Stirring effect

The stirring effect was studied at 0, 20, 50, 80 and 100 rpm under optimal conditions (Table 1). MB and MG initial concentrations were both 50 $mg{\cdot}L^{-1}$.

2.7. Adsorption kinetics and mechanism

The adsorption kinetics were analyzed using 0–300 min intervals under optimal conditions (Table 1). MB and MG initial concentrations were both 50 $mg{\cdot}L^{-1}$.

The results were analyzed using the pseudo-first-order (PFO) (Equation (4)), pseudo-second-order (PSO) (Equation (5)), and Elovich (Equation (6)) kinetic models. The adsorption mechanism was analyzed using the intraparticle diffusion model (Equation (7)).

$$q_t = q_e(1 - e^{-k_1 t}) \tag{4}$$

$$q_t = \frac{q_e^2 k_2 t}{1 + q_e k_2 t} \tag{5}$$

$$q_t = \frac{1}{\beta}\ln(1 + \alpha\beta t) \tag{6}$$

$$q_t = k_{di}\, t^{1/2} + C \tag{7}$$

where k_1 and k_2 are the PFO (min^{-1}) and PSO ($g{\cdot}mg^{-1}{\cdot}min^{-1}$) adsorption rate constants, respectively, α is the initial adsorption rate ($mg{\cdot}g^{-1}{\cdot}min^{-1}$), β is the desorption constant ($mg{\cdot}g^{-1}$), k_{di} is the mass transfer coefficient ($mg{\cdot}g^{-1}{\cdot}min^{-1/2}$), C is the constant associated with the boundary layer thickness ($mg{\cdot}g^{-1}$), and t is time (min).

2.8. Adsorption equilibrium

In the equilibrium study, samples containing dye concentrations of 10, 50, 100, 200, 300, 400 and 500 $mg{\cdot}L^{-1}$ were treated under optimal conditions (Table 1). Equilibrium was evaluated at temperatures of 20, 30 and 40 °C.

The equilibrium results were evaluated using the Freundlich (Equation (8)), Langmuir (Equation (9)), Temkin (Equation (10)) and Dubinin–Radushkevich (DR) (Equation (11)) adsorption isotherm models.

$$q_e = k_F C_e^{1/n} \tag{8}$$

$$q_e = \frac{q_{\max} k_L C_e}{1 + k_L C_e} \tag{9}$$

$$q_e = \frac{RT}{b}\ln(k_T C_e) \tag{10}$$

$$q_e = q_m \exp\left\{-k_{DR}\left[RT\ln\left(1+\frac{1}{C_e}\right)\right]^2\right\} \tag{11}$$

where k_F, k_L, k_T and k_{DR} are Freundlich ($mg{\cdot}g^{-1}$ ($mg{\cdot}L^{-1}$)), Langmuir ($L{\cdot}mg^{-1}$), Temkin ($L{\cdot}mg^{-1}$) and DR ($mol^2{\cdot}kJ^{-2}$) isotherm constants, n is the constant related to CaSF surface heterogeneity, q_{max} is the maximal adsorption capacity ($mg{\cdot}g^{-1}$), b is the constant related to the adsorption heat ($kJ{\cdot}mol^{-1}$), R is the universal constant of gases (8.314 J $mol^{-1}{\cdot}K^{-1}$), T is the process temperature (K), and q_m is the monolayer maximal adsorption capacity ($mg{\cdot}g^{-1}$).

The k_{DR} constant is associated with the mean adsorption energy (E), which can be calculated using Equation (12).

$$E = \frac{1}{\sqrt{2k_{DR}}} \tag{12}$$

The value of E enables the assessment of the nature of the process, whether it is physical adsorption ($E < 8$ $kJ{\cdot}mol^{-1}$), ion exchange ($8 < E < 16$ $kJ{\cdot}mol^{-1}$), or chemical adsorption ($E > 16$ $kJ{\cdot}mol^{-1}$) (Kaveeshwar *et al.* 2018).

2.9. Adsorption–desorption cycles

A preparation of 1 g of CaSF and 0.1 L of a 50 $mg{\cdot}L^{-1}$ MB solution was stirred at 80 rpm for 90 min, likewise, a preparation of 0.8 g of CaSF and 0.1 L of a 50 $mg{\cdot}L^{-1}$ MG solution (80 rpm, 90 min). The solutions were then filtered and the CaSF was washed with deionized water and dried. Then it was stirred with 0.1 L of ethanol 1:2 for 120 min for the desorption to occur. Three desorption cycles were run. The amount of dye desorbed (q_{des}) and the desorption efficiencies (%Desorption) were calculated using Equations (13) and (14, respectively.

$$q_{des} = \frac{C_e * V}{m} \tag{13}$$

$$\%\text{Desorption} = \left(\frac{q_{des}}{q_e}\right) \times 100 \tag{14}$$

3. RESULTS AND DISCUSSION

3.1. CaSF characterization

Both the morphological and the elemental analyses are important to understand the structure of CaSF and its principal elements before and after dye adsorption. Figure 1 presents the SEM of CaSF at different magnifications and Figure 2 shows the EDS results for CaSF before the adsorption of the dyes (a), after MB adsorption (b) and after MG adsorption (c).

Figure 1 shows that CaSF is amorphous. The anionic surfactant inhibits the formation of the crystalline phase of CaSF, while the nature of such inhibition depends on the concentration of the anionic surfactant in the solution (Bujan *et al.* 2001; Wei *et al.* 2004). As the concentration exceeded the critical micellar concentration, the anionic surfactant–Ca^{2+} interaction promoted miniature crystallization of CaSF, resulting in the formation of a few trigonal-shaped crystals (Figure 1).

According to the EDS results, CaSF is mainly composed of C (70.8%), Ca (17.1%) and O (10%) (Figure 2(a)). Figure 2(b) and 2(c) show that CaSF is able to adsorb both MB and MG, as there was an increase in C after adsorption (to 75.20 and 80.80%, respectively). The amount of Ca dropped in both cases, strongly indicating that the interaction between CaSF and the dyes results in the redissolution of Ca. Similar results were obtained in the removal of MB by flocculation–precipitation (Yang *et al.* 2016).

The FTIR spectra provide information about the functional groups present in CaSF that may be responsible for the adsorption of the dyes (see Figure 3).

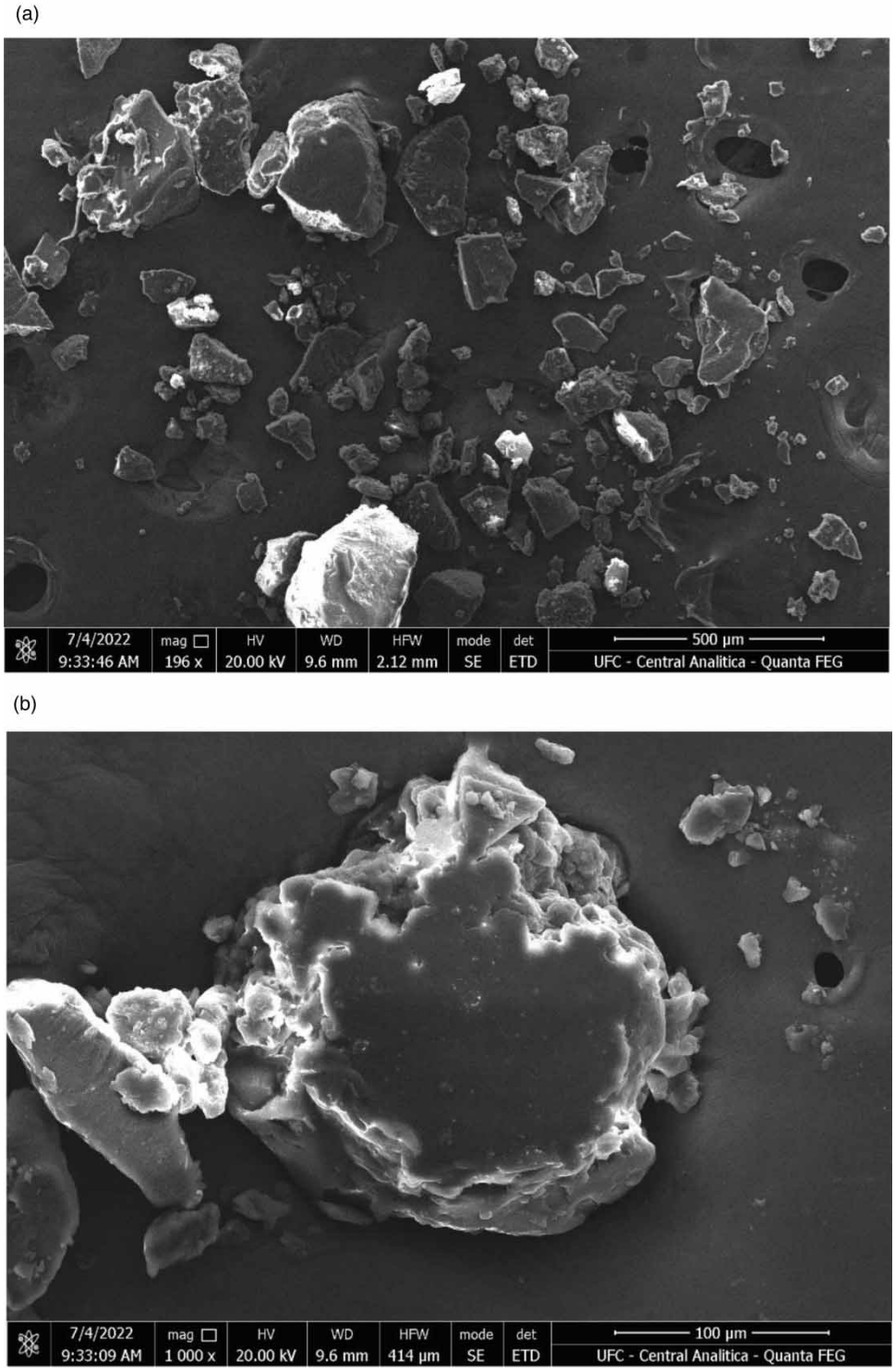

Figure 1 | (a) SEM of CaSF (196×). (b) SEM of CaSF (1000×).

The FTIR spectra (Figure 3) show some absorption peaks belonging to different functional groups, which was expected as CaSF is a complex compound. The peak at 3,417 cm^{-1} is typical of the elongation of the OH^- functional group and indicates the presence of hydrogen bonds. The peak at 3,011 cm^{-1} is typical of simple unsaturated olefinic compounds (C = C). The peaks at 2,921–2,850 cm^{-1} correspond to the stretching of linear long-chain aliphatic compounds (C–H). The relative high intensity of these peaks points to the fact that CaSF has no ramifications in its molecular structure (Mirghani *et al.* 2002; Nandiyanto *et al.* 2019).

(a)

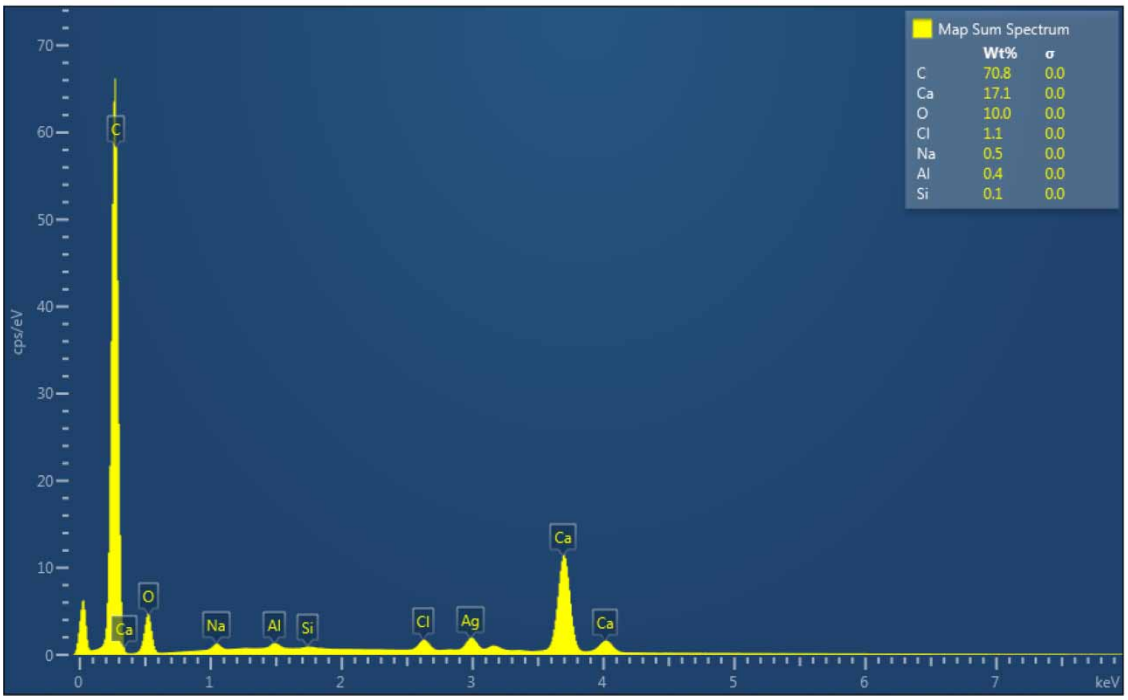

Figure 2 | (a) EDS of CaSF before dye adsorption. (b) EDS of CaSF after MB adsorption. (c) EDS of CaSF after MG adsorption. (*continued.*).

The peak at 1,693 cm^{-1} indicates alkenyl stretch (C = C), while the sequence of peaks at 1,578–1,541 and 1,432–1,420 cm^{-1} suggests the presence of carbonyl (C = O) groups in the form of carboxylate or carboxylic acid salt. The peak at 1,113 cm^{-1} indicates the presence of ester (COO). Finally, the peaks at 722–675 cm^{-1} indicate the deformation of olefins group (C–H) (Mirghani *et al.* 2002; Nandiyanto *et al.* 2019).

These functional groups can form surface complexes or bonds with the dye molecules and, consequently, promote their adsorption onto the surface of CaSF. The comparison between the CaSF FTIR spectra before and after dye adsorption shows that, after the adsorption, there were changes in the intensities of the absorption peaks mentioned above. Therefore, the functional groups concerned influence MB and MG adsorption on CaSF. Similar results were found for the removal of methyl red from aqueous matrices using CaSF (Teixeira *et al.* 2023).

Figure 4 presents the pH_{PZC} results for CaSF. The pH_{PZC} was determined through the arithmetic mean of the final pH values within the buffer zone.

The study pH_{PZC} makes it possible to find the ideal pH for the adsorption process of dyes on CaSF to occur. Figure 4 shows that CaSF has a buffer zone, or the point of zero charge, at pH values between 3 and 8 (circled in red). Therefore, the pH_{PZC} of CaSF is 6. Anion adsorption is favored at pHs below the pH_{PZC}, while cation adsorption is favored at pHs above it (Kumar *et al.* 2010). MB and MG are both cationic, so their adsorption is favored when the pH exceeds the pH_{PZC}. The ideal pH defined for the process was 7, thus eliminating the need for sample buffering or pH adjustment.

3.2. CaSF dosage

The study of CaSF dosage is essential to optimize the amount of adsorbent used, so that maximal removal efficiency is achieved and problems such as adsorbent excess or unsaturation are avoided. Figure 5 presents the CaSF dosage results.

Figure 5 shows that CaSF is more efficient in removing MG than MB and that the dosage influences the process. The observed trend was that removal efficiency increases with increasing CaSF dosage for both dyes until the optimal dose is attained. Dosages above optimal do not significantly affect removal efficiency.

The lowest MB removal efficiency (53%) was achieved at the lowest CaSF dosage (1 $g{\cdot}L^{-1}$), while the highest (84%) was achieved at 10 $g{\cdot}L^{-1}$, as above the dosage removal efficiency does not change. Therefore, the optimal CaSF dosage for MB is 10 $g{\cdot}L^{-1}$ and was used to evaluate the other test parameters.

(b)

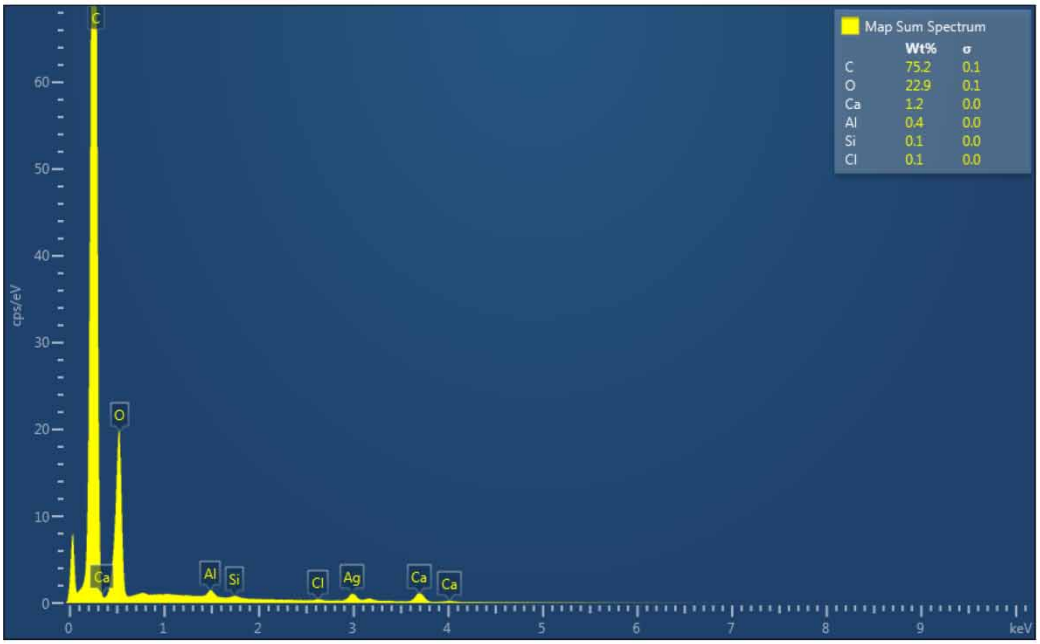

(c)

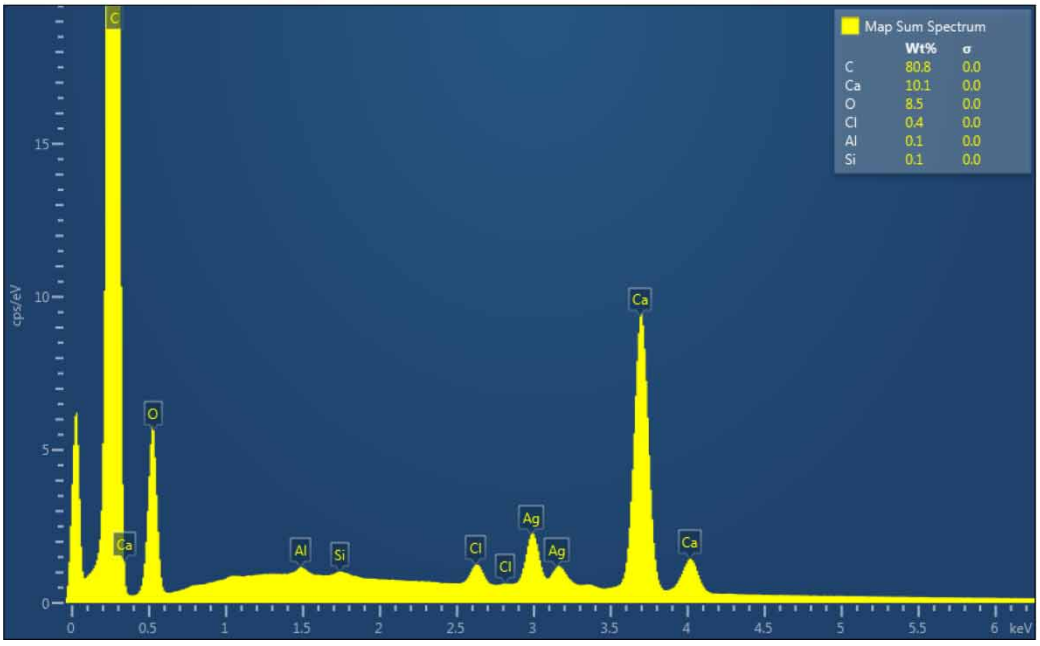

Figure 2 | Continued.

The lowest MG removal efficiency (86%) was achieved at the lowest CaSF dosage (1 g·L^{-1}), while the highest efficiency (100%) was achieved at 8 g·L^{-1}, as above the removal efficiency does not change. Therefore, the optimal CaSF dosage for MG is 8 g·L^{-1}, and it was the one used for the evaluation of the other tested parameters.

As the CaSF dosage increases, the availability of active adsorption sites also increases and, consequently, dye removal efficiency also increases. Dosages above established optimal values, in addition to not increasing efficiency, promote unsaturation of active adsorption sites, causing waste of CaSF.

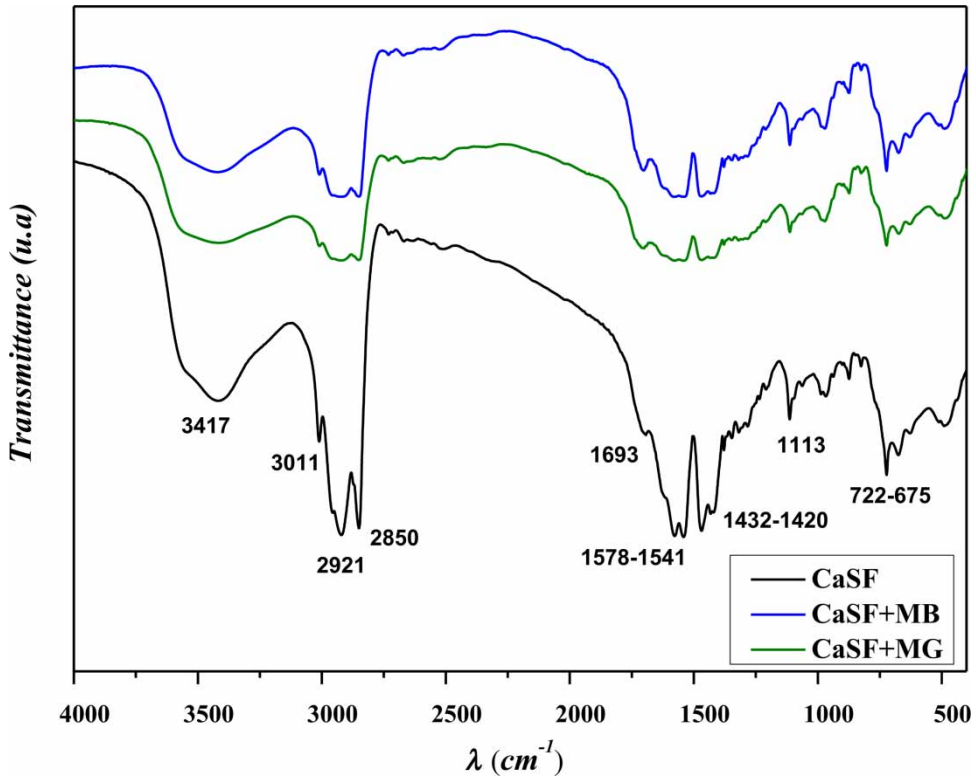

Figure 3 | CaSF FTIR spectra.

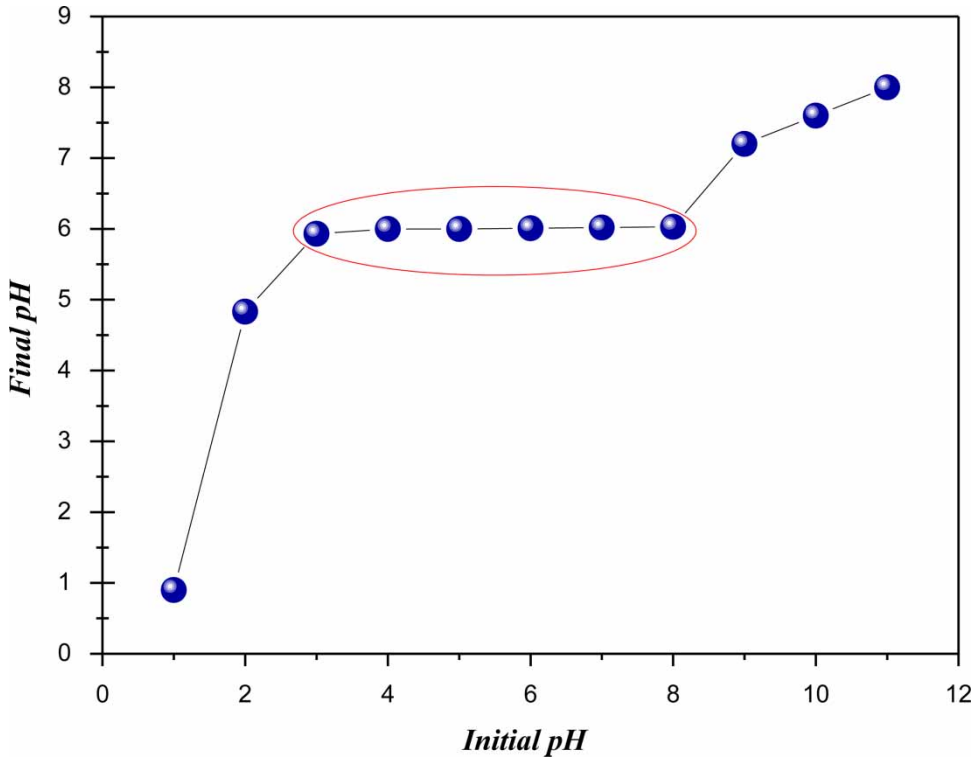

Figure 4 | Determination of the pH_{PZC}. Please refer to the online version of this paper to see this figure in colour: http://dx.doi.org/10.2166/wpt.2023.021.

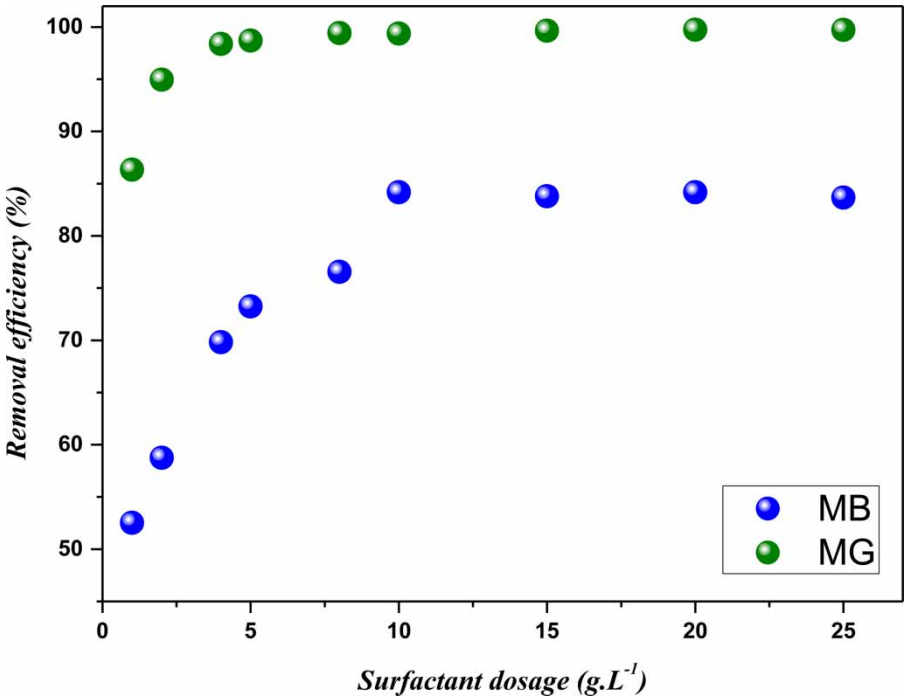

Figure 5 | Dosage effect (MB–MG at 50 mg·L^{-1}, 90 min, pH = 7, 80 rpm, 20 °C).

3.3. Stirring

The study of the stirring effect is important as it provides the stirring rate that maximizes free dye transfer from the effluent to the CaSF (Figure 6).

Stirring influences the adsorption of both dyes (Figure 6) as the removal efficiency varied with the variation of the stirring rate until an equilibrium was reached. For MB, the process carried out without stirring (0 rpm) was able to remove 69%, while for MG there was a removal of 62%. When stirring was increased to 20 rpm, the MB and MG removal rates increased to 82 and 97%, respectively, indicating that the MG adsorption process is more dependent on stirring than that of MB.

The optimal stirring rate was 80 rpm for both dyes, showing removal rates of 84 and 100% for MB and MG, respectively. Stirring rates above 80 rpm showed no increase in the removal efficiency.

As the stirring rate is increased, the CaSF adsorption sites become more accessible due to the increased turbulence. Consequently, there is a decrease in the thickness of the liquid film around the CaSF particles and an increase in the diffusion of dye molecules through it, generating an increase in the mass transfer of free MB and MG in solution to the CaSF surface. After reaching the optimal condition, more aggressive stirring becomes unnecessary and can be avoided in order to save energy and material costs.

3.4. Adsorption kinetics

The analysis of the adsorption kinetics improves understanding of the free dye molecule mass transfer to the CaSF surface over time. Furthermore, it makes it possible to find the time required for equilibrium to be reached and indicates the type of adsorption taking place. Figure 7 and Table 2 provide the adsorption kinetics results.

Figure 7 shows that the adsorption of both dyes occurs very quickly in the first 20 min and then decelerates until reaching equilibrium at 90 min. The high early adsorption rate is due to the high availability of free sites on the CaSF surface. After 20 min, adsorption is slower because CaSF site availability has decreased considerably and those dye molecules already adsorbed tend to repel free dye molecules in solution (Oyelude *et al.* 2018).

Table 2 shows that for MB, the PSO model best fitted the experimental data, presenting the highest determination coefficient ($R_{adj}^2 = 0.99$), the lowest error (RSS = 0.10), and q_e closest to the experimental equilibrium adsorption capacity (q_{e_exp}).

For MG, the PFO model best fitted the experimental data ($R_{adj}^2 = 0.99$ and RSS = 0.70). The PSO model also fitted the MG data but was not the best fit. The Elovich model did not fit either dataset ($R_{adj}^2 < 0.95$). The fact that

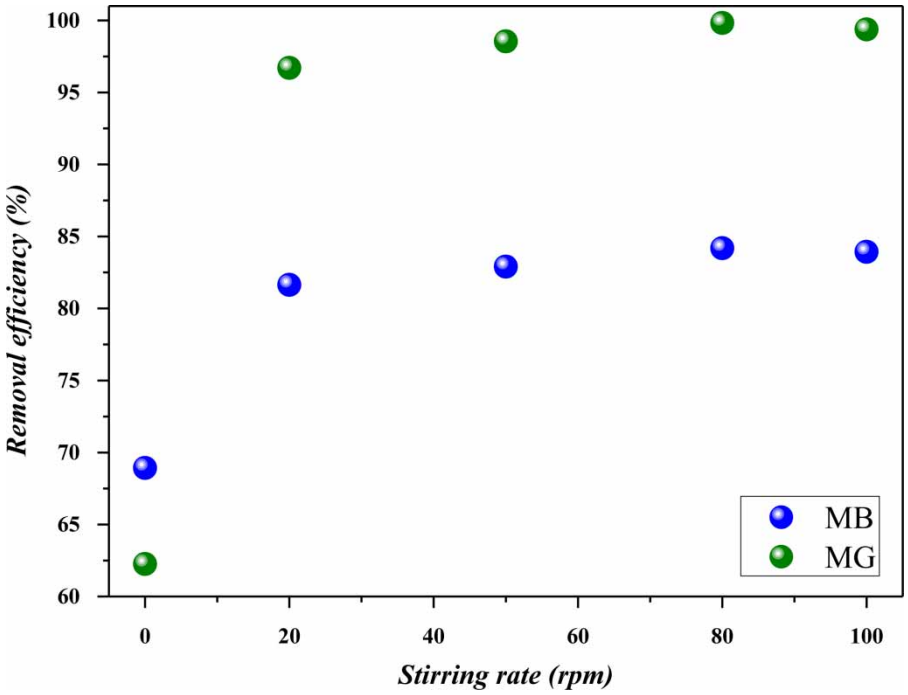

Figure 6 | Stirring effect (MB–MG at 50 mg·L^{-1}, 90 min, pH = 7, 20 °C).

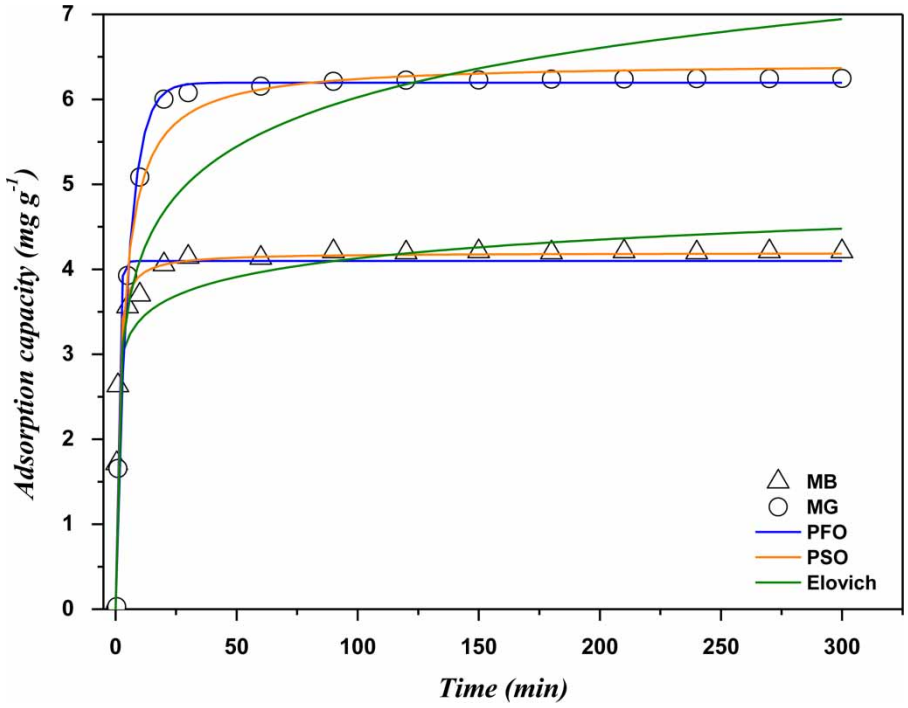

Figure 7 | Experimental results and modeling of the adsorption kinetics for both dyes (MB–MG at 50 mg·L^{-1}, pH = 7, 80 rpm, 20 °C).

the PSO model fits both dyes is a strong indication that chemisorption governs the process. It also indicates that physisorption may occur during in the early stages, which explains that the PFO model also fits the process. Zhang *et al.* (2017) obtained similar results using hydrochar derived from algal residues.

Table 2 | Adsorption kinetics model parameters (both dyes)

		PFO				PSO				Elovich			
MB	q_{e_exp} (mg g^{-1})	q_e (mg g^{-1})	k_1 (min^{-1})	R_{adj}^2	RSS	q_e (mg g^{-1})	k_2 (g mg^{-1}/min^{-1})	R_{adj}^2	RSS	α (mg·g^{-1}·min^{-1})	β (mg·g^{-1})	R_{adj}^2	RSS
	4.21	4.10	1.04	0.97	0.52	4.19	0.35	0.99	0.10	1,427.68	3.15	0.93	1.38
		PFO				**PSO**				**Elovich**			
MG	q_{e_exp} (mg g^{-1})	q_e (mg g^{-1})	k_1 (min^{-1})	R_{adj}^2	RSS	q_e (mg g^{-1})	k_2 (g mg^{-1}/min^{-1})	R_{adj}^2	RSS	α (mg·g^{-1}·min^{-1})	β (mg·g^{-1})	R_{adj}^2	RSS
	6.24	6.20	0.19	0.99	0.70	6.43	0.05	0.98	1.10	11.11	1.19	0.88	8.90

Table 3 | Adsorption isotherm model parameters for both dyes at different temperatures (90 min, pH = 7, 80 rpm)

			Langmuir				DR				
Dye	***T* (°C)**	**q_{max_exp} (mg·g^{-1})**	**q_{max} (mg·g^{-1})**	**k_L (L·mg^{-1})**	**R_{adj}^2**	**RSS**	**q_m (mg·g^{-1})**	**k_{DR} (mol²·kJ^{-2})**	***E* (kJ·mol^{-1})**	**R_{adj}^2**	**RSS**
MB	20	42.73	136	0.006	0.99	10.85	40	6.62E-05	86.91	0.93	91.75
	30	43.44	199	0.004	0.99	9.01	49	1.07E-04	68.36	0.94	99.06
	40	41.58	142	0.005	0.99	2.48	40	8.42E-05	77.06	0.92	95.86
			Temkin					**Freundlich**			
			***b* (J·mol^{-1})**	**k_T (L·mg^{-1})**	**R_{adj}^2**	**RSS**		**k_F (L·mg^{-1})**	***n***	**R_{adj}^2**	**RSS**
	20	42.73	261.42	0.49	0.76	298.60		1.22	1.21	0.98	13.54
	30	43.44	241.87	0.48	0.77	405.99		1.13	1.14	0.98	12.58
	40	41.58	339.94	0.71	0.67	372.24		1.06	1.20	0.98	5.68
			Langmuir				**DR**				
MG		**q_{max_exp} (mg·g^{-1})**	**q_{max} (mg·g^{-1})**	**k_L (L·mg^{-1})**	**R_{adj}^2**	**RSS**	**q_m (mg·g^{-1})**	**k_{DR} (mol²·kJ^{-2})**	***E* (kJ·mol^{-1})**	**R_{adj}^2**	**RSS**
	20	62.38	92	2.79	0.92	222.34	76	5.65E-09	9,407.21	0.95	119.79
	30	62.39	95	2.56	0.86	366.49	78	4.25E-08	3,429.97	0.91	235.94
	40	62.42	123	1.60	0.97	90.40	75	3.87E-08	3,594.43	0.97	91.84
			Temkin					**Freundlich**			
			***b* (J·mol^{-1})**	**k_T (L·mg^{-1})**	**R_{adj}^2**	**RSS**		**k_F (L·mg^{-1})**	***n***	**R_{adj}^2**	**RSS**
	20	62.38	189.91	76.35	0.73	721.67		71.91	1.85	0.84	422.96
	30	62.39	200.39	76.51	0.65	918.26		72.67	1.80	0.79	556.61
	40	62.42	201.36	74.93	0.75	675.16		88.63	1.40	0.96	106.17

3.5. Adsorption equilibrium

The study of the equilibrium at different temperatures through adsorption isotherms can provide parameters such as CaSF's maximal adsorption capacity and the type of adsorption involved (physisorption or chemisorption). It can also indicate whether it is the endothermic or exothermic proces (Table 3).

As can be seen, the temperature does not influence CaSF's adsorption of MB, as it has little effect on the experimental adsorption capacity (q_{max_exp}). The increase in q_{max_exp} and q_{max} with temperature increase from 20 to 30 °C indicates that the process is endothermic. The Langmuir model best fitted the experimental data, with $R_{adj}^2 = 0.99$ and lower error values (RSS), showing a q_{max} of 199 mg·g^{-1} at 30 °C. Therefore, the adsorption of MB occurs on a monolayer with a defined number of sites of equivalent energies (Nascimento *et al.* 2020).

Likewise, the temperature does not influence MG adsorption by CaSF, as the q_{max_exp} did varied little with increasing temperature. The Langmuir model showed the highest q_{max} value at 40 °C (123 mg·g^{-1}), indicating that the process is endothermic. However, the DR model, which best fits the data, indicates that CaSF's MG adsorption occurs in a multilayered and heterogeneous way (Ruthven 1984; Bonilla-Petriciolet *et al.* 2017). The values of E (>16 kJ·mol^{-1}) presented in the DR model indicate that for both dyes, the process is one of chemisorption (Kaveeshwar *et al.* 2018).

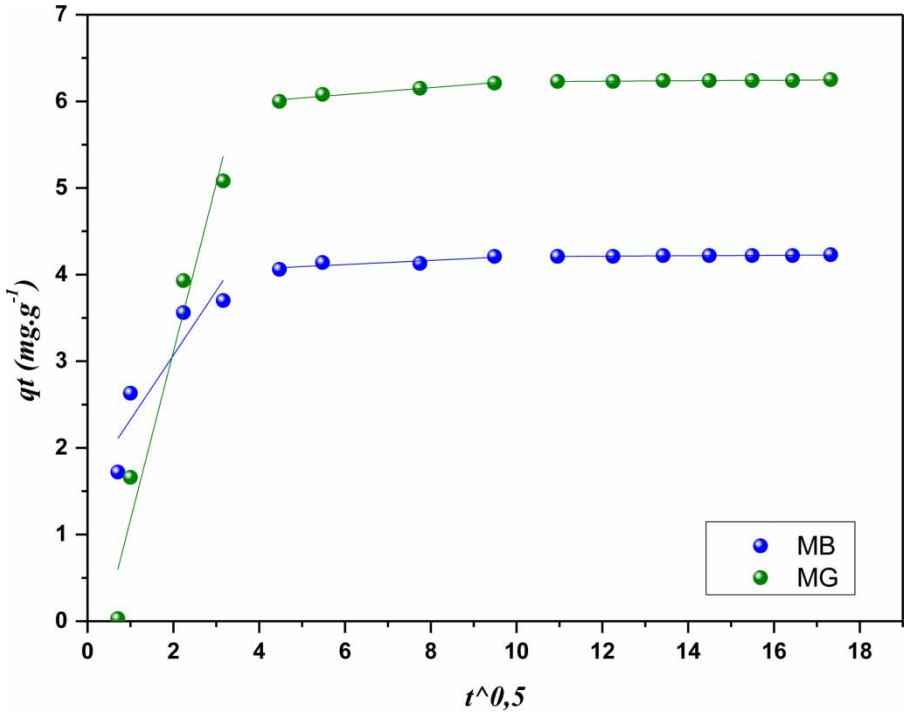

Figure 8 | Intraparticle diffusion model.

Table 4 | Intraparticle diffusion model parameters

Dye	Concentration (mg·L^{-1})	q_{e_exp} (mg·g^{-1})	Intraparticle diffusion				
			Step	C (mg·g^{-1})	k_{di} (mg·g^{-1}·min$^{-0.5}$)	R_{adj}^2	RSS
MB	50	4.21	I	1.58	0.74	0.77	0.40
			II	3.97	0.02	0.66	3E-3
			III	4.18	2.70E-3	0.76	5.73E-5
MG	50	6.24	I	0.77	1.94	0.92	0.78
			II	5.84	3.84E-2	0.95	8.65E-4
			III	6.20	2.70E-3	0.76	5.74E-5

The fact that temperature does not influence the process indicates that CaSF is stable with respect to temperature variation. Similar results were obtained with the removal of Disperse Blue 56 (Melo *et al.* 2021) and Yellow 27 (Melo *et al.* 2017) using ionic flocculation.

3.6. Adsorption mechanism

According to the intraparticle diffusion model, adsorption can occur in one or more steps. If the q_t vs. $t^{0.5}$ plot touches the origin, adsorption is governed by intraparticle diffusion. Otherwise, it occurs in two or more steps. External surface adsorption (on the film) takes place in the first, intraparticle diffusion controls the adsorption rate in the second, and the third is equilibrium, in which the adsorbate (dye) concentration is extremely low (Weber & Morris 1963). Figure 8 and Table 4 provide the results obtained in this study.

Figure 8 shows that no point touches the origin of the graph for either dye, indicating that their adsorption by CaSF involves two or more steps. The increase of the constant C at each step indicates an increase of the boundary layer effect in the process and also suggests that more than one mechanism is involved as a limiting factor in the adsorption of dye (Teixeira *et al.* 2022a, 2022b).

For both dyes (Table 4), k_{di} has the highest value in the first step. The third step, equilibrium, has the lowest k_{di} values, yet without representing an adsorption limiting factor (Melo *et al.* 2017). The second step, corresponding to intraparticle diffusion, presents the lowest values of k_{di}, a strong indication that this step controls the process. Similar results were found in MG removal by ionic flocculation (Teixeira *et al.* 2022a, 2022b).

3.7. Adsorption–desorption cycles

The study of the adsorption–desorption cycles was used to evaluate the regeneration capacity of CaSF, as well as the number of cycles over which CaSF maintains a high removal efficiency. In addition, this study also gives another indication about the type of adsorption taking place in the process (Figures 9 and 10).

Figure 9 shows that, after three cycles, MB removal efficiency decreased from 84 to 61%. The same happened to the desorption efficiency, which dropped from 52 to 22%, and to the adsorption capacity of CaSF, which also dropped from 4.6 to 3.1 mg·g^{-1}. Likewise, Figure 10 shows that, for MG, in the first two cycles CaSF maintained its dye and desorption efficiencies and its adsorption capacity (100%, 8% and 6.2 mg·g^{-1}, respectively). In the third cycle, MG removal efficiency dropped to 70%, desorption efficiency to 6%, and adsorption capacity to 4.4 mg·g^{-1}. The low desorption efficiency of both dyes is a strong indication that chemisorption is the process involved, confirming the DR isotherm's E values.

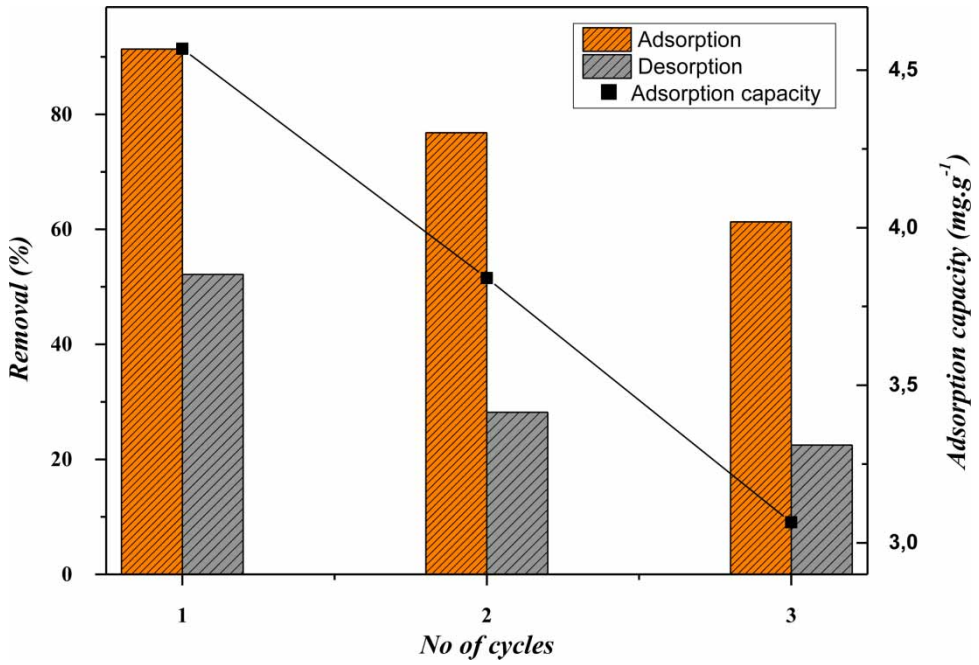

Figure 9 | MB adsorption–desorption cycles.

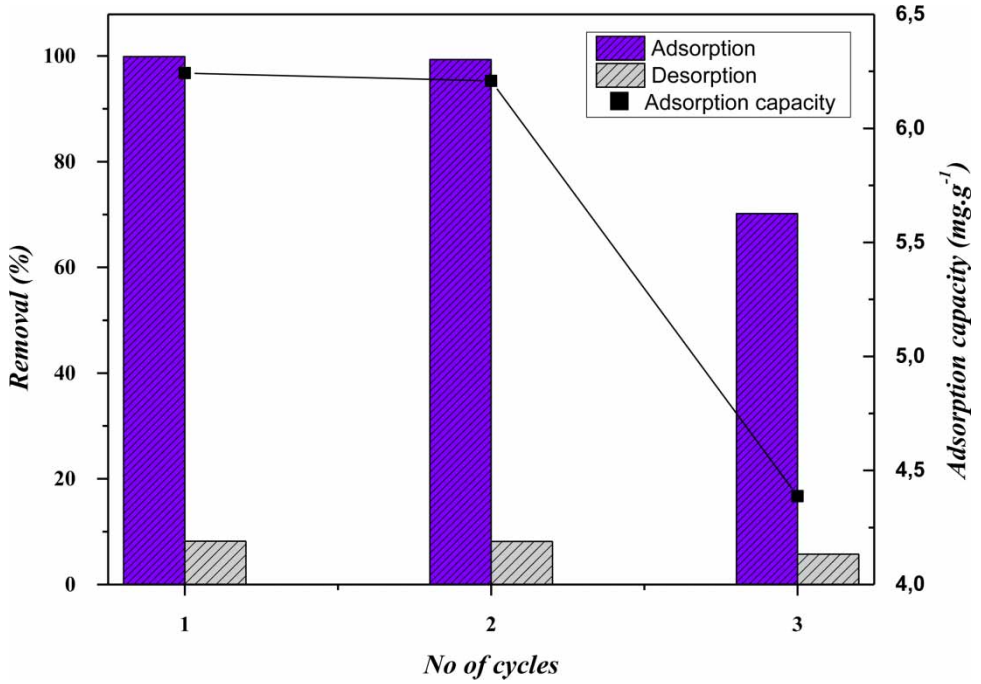

Figure 10 | MG adsorption–desorption cycles.

Regeneration becomes more difficult with each cycle because the dye–CaSF interaction increases, that is, the strength of the bonds involved increases, making dye desorption increasingly difficult, eventually leading to saturation of the CaSF and to decreasing adsorption capacity. Even after three cycles of CaSF, however, it showed good removal efficiency (>60%), indicating that it can be used as an adsorbent for both MB and MG.

4. CONCLUSION

CaSF obtained from frying soybean oil is amorphous and contains functional groups such as OH^- and C = O, that favor cationic dye adsorption. The pH_{PZC} CaSF is 6, indicating that a pH 7 (neutral) can be used as the optimal for the process, thus avoiding the need to adjust the effluent's pH. The optimal CaSF dosage removal efficiency was 10 $g{\cdot}L^{-1}$ for MB and 8 $g{\cdot}L^{-1}$ for MG. Stirring affects the process and MG is more sensitive to this than MB. The equilibrium time for both dyes was 90 min. Adsorption capacity varied little with temperature and dye adsorption appears to be endothermic.

The PSO model fitted the MB kinetics data best, while the PFO model was best for MG. The Langmuir and the DR isotherm models were the best fit for MB and MG adsorption, respectively. The adsorption mechanism study indicated that the process has more than one step and that intraparticle diffusion controls adsorption for both dyes. The adsorption–desorption cycle study showed dye removal efficiency above 60% for up to three cycles.

ACKNOWLEDGEMENTS

The authors would like to acknowledge the financial support for this work of Cearense Foundation for Scientific and Technological Development Support – FUNCAP, BPI (Grant N◦ BP3-0139-00276.01.00/18 and N◦ BP4-0172-00080.01.00/20) and Central Analítica of the Federal University of Ceará (UFC).

AUTHOR CONTRIBUTIONS

Y.N.T. investigated and validated the article, developed the methodology, and wrote the original draft. F.J.d.P.F. conceptualized the whole article, conducted funding acquisition and formal analysis, brought resources, wrote the review and edited the article, and administered the project. V.P.B. developed the methodology and conducted formal analysis. J.M.C.M. did formal analysis and wrote the review and edited the article. D.B.S. and J.V.S.N. visualized the article and conducted methodology and formal analysis. J.d.Q.d.S. and R.N.P.T. visualized the article and did formal analysis.

DATA AVAILABILITY STATEMENT

All relevant data are included in the paper or its Supplementary Information.

CONFLICT OF INTEREST

The authors declare there is no conflict.

REFERENCES

Anirudhan, T. S. & Ramachandran, M. 2015 Adsorptive removal of basic dyes from aqueous solutions by surfactant modified bentonite clay (organoclay): kinetic and competitive adsorption isotherm. *Process Safety Environmental Protection* **95**, 215–225. https://doi.org/10.1016/j.psep.2015.03.003.

Benosmane, N., Boutemeur, B., Hamdi, S. M. & Hamdi, M. 2022 Removal of methylene blue dye from aqueous solutions using polymer inclusion membrane technology. *Applied Water Science* **12**(104), 1–11. https://doi.org/10.1007/s13201-022-01627-1.

Bonilla-Petriciolet, A., Mendonza-Castillo, D. I. & Reynel-Ávila, H. E. 2017 *Adsorption Processes for Water Treatment and Purification*. Springer, Gewerbestrasse.

Bujan, M., Sikiric, M., Filipovic-Vincekovic, N., Vdovic, N., Garti, N. & Füredi-Milhofer, H. 2001 Effect of anionic surfactants on crystal growth of calcium hydrogen phosphate dihydrate. *Langmuir* **17**(21), 6461–6470. https://doi.org/10.1021/la0107190.

Crini, G. & Badot, P. 2008 Application of chitosan, a natural aminopolysaccharide, for dye removal from aqueous solutions by adsorption processes using batch studies: a review of recent literature. *Progress in Polymer Science* **33**(4), 399–447. https://doi.org/10.1016/j.progpolymsci.2007.11.001.

Giri, B. S., Sonwani, R. K., Varjani, S., Chaurasia, D., Varadavenkatesan, T., Chaturvedi, P., Yadav, S., Katiyar, V., Singh, R. S. & Pandey, A. 2022 Highly efficient bio-adsorption of malachite green using Chinese Fan-Palm Biochar (*Livistona chinensis*). *Chemosphere* **287**(3), 1–11. https://doi.org/10.1016/j.chemosphere.2021.132282.

Kaveeshwar, A. R., Kumar, P. S., Revellame, E. D., Gang, D. D., Zappi, M. E. & Subramaniam, R. 2018 Adsorption properties and mechanism of barium (II) and strontium (II) removal from fracking wastewater using pecan shell based activated carbon. *Journal of Cleaner Production* **193**, 1–13. https://doi.org/10.1016/j.jclepro.2018.05.041.

Khatri, A. & Rana, P. S. 2020 Visible light assisted photocatalysis of methylene blue and Rose Bengal dyes by iron doped NiO nanoparticles prepared via chemical co-precipitation. *Physica B: Condensed Matter* **579**(411905), 1–8. https://doi.org/10.1016/j.physb.2019.411905.

Kumar, P., Sudha, S., Chand, S. & Srivastava, V. C. 2010 Phosphate removal from aqueous solution using coir pith activated carbon. *Separation Science and Technology* **45**(10), 1463–1470. https://doi.org/10.1080/01496395.2010.485604.

Lee, Y. C., Kim, E. J., Yang, J. W. & Shin, H. J. 2011 Removal of malachite green by adsorption and precipitation using aminopropyl functionalized magnesium phyllosilicate. *Journal of Hazardous Materials* **192**(1), 62–70. https://doi.org/10.1016/j.jhazmat.2011.04.094.

Li, Q., Li, Y., Ma, X., Du, Q., Suik, W. D., Wang, C., Li, H. & Xia, Y. 2017 Filtration and adsorption properties of porous calcium alginate membrane for methylene blue removal from water. *Chemical Engineering Journal* **316**, 623–630. https://doi.org/10.1016/j.cej.2017.01.098.

Mariana, M., Mistar, E. K., Alfatah, T. & Supardan, M. D. 2021 High-porous activated carbon derived from *Myristica fragrans* shell using one-step KOH activation for methylene blue adsorption. *Bioresource Technology Reports* **16**, 1–11. https://doi.org/10.1016/j.biteb.2021.100845.

Mayani, V. J., Mayani, S. V. & Kim, S. W. 2017 A sustainable nanocomposite Au(Salen)@CC for catalytic degradation of Eosin y and Chromotrope 2R dyes. *Scientific Reports* **7**(7239), 1–9. https://doi.org/10.1038/s41598-017-07707-6.

Melo, R. P. F., Barros Neto, E. L., Moura, M. C. P. A., Dantas, T. N. C., Neto, A. A. D. & Nunes, S. K. S. 2017 Removal of direct Yellow 27 dye by ionic flocculation: the use of an environmentally friendly surfactant. *Journal of Surfactants and Detergents* **20**(2), 459–465. https://doi.org/10.1007/s11743-016-1913-9.

Melo, R. P. F., Carmo, S. K. S., Barros, E. L. B., Câmara, A. G., Nunes, S. K. S. & Barros Neto, E. L. 2021 Removal of Disperse Blue 56 from synthetic textile effluent using ionic flocculation. *Water Science & Technology* **83**(11), 2714–2723. https://doi.org/10.2166/wst.2021.173.

Mirghani, M. E. S., Che Man, Y. B., Jinap, S., Baharin, B. S. & Bakar, J. 2002 FTIR spectroscopic determination of soap in refined vegetable oils. *Journal of the American Oil Chemist's Society* **79**(2), 111–116. https://doi.org/10.1007/s11746-002-0443-4.

Mortada, W. I. 2020 Recent developments and applications of cloud point extraction: a critical review. *Microchemical Journal* **157**(105055), 1–13. https://doi.org/10.1016/j.microc.2020.105055.

Mouni, L., Belkhiri, L., Bollinger, J. C., Bouzaza, A., Assadi, A., Tirri, A., Dahmoune, F., Madani, K. & Remini, H. 2018 Removal of methylene blue from aqueous solutions by adsorption on Kaolin: kinetic and equilibrium studies. *Applied Clay Science* **153**, 38–45. https://doi.org/10.1016/j.clay.2017.11.034.

Nandiyanto, A. B. D., Oktiani, R. & Ragadhita, R. 2019 How to read and interpret FTIR spectroscope of organic material. *Indonesian Journal of Science & Technology* **4**(1), 97–118. https://doi.org/10.17509/ijost.v4i1.15806.

Nascimento, R. F., Lima, A. C. A., Vidal, C. B., Melo, D. Q. & Raulino, G. S. C. 2020 *Adsorção Aspectos teóricos e aplicações ambientais (Adsorption Theoretical Aspects and Environmental Applications)*. Book, Fortaleza, Brazil.

Novais, R. M., Ascensão, G., Tobaldi, D. M., Seabra, M. P. & Labrincha, J. A. 2018 Biomass fly ash geopolymer monoliths for effective methylene blue removal from wastewaters. *Journal of Cleaner Production* **171**, 783–794. https://doi.org/10.1016/j.jclepro.2017.10.078.

Oyelude, E. O., Awudza, J. A. M. & Twumasi, S. K. 2018 Removal of malachite green from aqueous solution using pulverized teak leaf litter: equilibrium, kinetic and thermodynamic studies. *Chemistry Central Journal* **12**(81), 1–10. https://doi.org/10.1186/s13065-018-0448-8.

Petcu, A. R., Lazar, C. A., Rogozea, E. A., Olteanu, N. L., Meghea, A. & Mihaly, M. 2016 Nonionic microemulsion systems applied for removal of ionic dyes mixtures from textile industry wastewaters. *Separation and Purification Technology* **158**, 155–159. https://doi.org/10.1016/j.seppur.2015.12.002.

Peydayesh, M. & Rahbar-Kelishami, A. 2015 Adsorption of methylene blue onto *Platanus orientalis* leaf powder: kinetic, equilibrium and thermodynamic studies. *Journal of Industrial and Engineering Chemistry* **21**, 1014–1019. https://doi.org/10.1016/j.jiec.2014.05.010.

Robles, J. O. & Regalbuto, J. R. 2004 *The Engineering of Pt/Carbon Catalyst Preparation for Application on Proton Exchange Fuel Cell Membrane (PEFCM)*. Available from: https://amrel.bioe.uic.edu/NSFREU2004/Reports2004/Jaime%20Robles_Final%20Report.pdf (accessed 31 January 2023).

Ruthven, D. M. 1984 *Principles of Adsorption and Adsorption Process*. John Wiley & Sons, New York.

Salamat, S., Hadavifar, M. & Rezaei, H. 2019 Preparation of nanochitosan-STP from shrimp shell and its application in removing of malachite green from aqueous solutions. *Journal of Environmental Chemical Engineering* **7**(5), 1–8. https://doi.org/10.1016/j.jece.2019.103328.

Sharma, G., Gupta, V. K., Agarwal, S., Kumar, A., Thakur, S. & Pathania, D. 2016 Fabrication and characterization of Fe@MoPO nanoparticles: ion exchange behavior and photocatalytic activity against malachite green. *Journal of Molecular Liquids* **219**, 1137–1143. https://doi.org/10.1016/j.molliq.2016.04.046.

Sun, Y., Zhang, Y., Li, W., Zhang, W., Xu, Z., Dai, M. & Zhao, G. 2021 Combination of the endophytic manganese-oxidizing bacterium *Pantoea eucrina* SS01 and biogenic Mn oxides: an efficient and sustainable complex in degradation and detoxification of malachite green. *Chemosphere* **280**(130785), 1–10. https://doi.org/10.1016/j.chemosphere.2021.130785.

Teixeira, Y. N., Melo, R. P. F., Fernandes, M. R., Carmo, S. K. S. & Barros Neto, E. L. 2022a Malachite green removal using ionic flocculation. *Water Practice & Technology* **17**(5), 1113–1128. https://doi.org/10.2166/wpt.2022.054.

Teixeira, Y. N., Paula Filho, F. J., Bacurau, V. P., Menezes, J. M. C., Fan, A. Z. & Melo, R. P. F. 2022b Removal of Methylene Blue from a synthetic effluent by ionic flocculation. *Helyion* **8**(10), e10868. https://doi.org/10.1016/j.heliyon.2022.e10868.

Teixeira, Y. N., Menezes, J. M. C., Teixeira, R. N. P., Paula Filho, F. J. & Oliveira, T. M. B. F. 2023 Eco-friendly anionic surfactant for the removal of methyl red from aqueous matrices. *Textiles* **3**(1), 52–65. https://doi.org/10.3390/textiles3010005.

Verma, A., Thakur, S., Mamba, G., Prateek, Gupta, R. K., Thakur, P. & Thakur, V. K. 2020 Graphite modified sodium alginate hydrogel composite for efficient removal of malachite green dye. *International Journal of Biological Macromolecules* **148**, 1130–1139. https://doi.org/10.1016/j.ijbiomac.2020.01.142.

Weber, W. J. & Morris, J. C. 1963 Kinetics of adsorption on carbon from solution. *Journal of the Sanitary Engineering Division* **89**(2), 31–59. https://doi.org/10.1061/JSEDAI.0000430.

Wei, H., Shen, Q., Zhao, Y., Wang, D. & Xu, D. 2004 Crystallization habit of calcium carbonate in the presence of sodium dodecyl sulfate and/or polypyrrolidone. *Journal of Crystal Growth* **260**(3–4), 511–516. https://doi.org/10.1016/j.jcrysgro.2003.08.047.

Yang, Z., Li, M., Yu, M., Huang, J., Xu, H., Zhou, Y., Song, P. & Xu, R. 2016 A novel approach for methylene blue removal by calcium dodecyl sulfate enhanced precipitation and microbial flocculant GA1 flocculation. *Chemical Engineering Journal* **303**, 1–13. https://doi.org/10.1016/j.cej.2016.05.101.

Zhang, H., Zhang, F. & Huang, Q. 2017 Highly effective removal of malachite green from aqueous solution by hydrochar derived from phycocyaninextracted algal bloom residues through hydrothermal carbonization. *RSC Advances* **7**, 5790–5799. https://doi.org/10.1039/C6RA27782A.

Zhou, W., Huang, J., Li, J., Xu, Z., Cao, L., Yao, C. & Lu, J. 2015 Cr_2WO_6 nanoparticles prepared by hydrothermal assisted method with selective adsorption properties for methylene blue in water. *Materials Science in Semiconductor Processing* **34**, 170–174. https://doi.org/10.1016/j.mssp.2015.02.010.

Zhu, S., Fang, S., Huo, M., Yu, Y., Chen, Y., Yang, X., Geng, Z., Wang, Y., Bian, D. & Huo, H. 2015 A novel conversion of the groundwater treatment sludge to magnetic particles for the adsorption of methylene blue. *Journal of Hazardous Materials* **292**, 173–179. https://doi.org/10.1016/j.jhazmat.2015.03.028.

First received 9 November 2022; accepted in revised form 5 February 2023. Available online 22 February 2023